Internal wave attractors in 3D geometries : A dynamical systems approach[☆]

Grimaud Pillet [a], Leo R.M. Maas [b], Thierry Dauxois [a,*]

[a] *Université de Lyon, ENS de Lyon, UCBL, CNRS, Laboratoire de Physique, Lyon, France*
[b] *Institute for Marine and Atmospheric Research Utrecht, Utrecht University, Netherlands*

A B S T R A C T

We study the propagation in three dimensions of internal waves using ray tracing methods and traditional dynamical systems theory. The wave propagation on a cone that generalizes the Saint Andrew's cross justifies the introduction of an angle of propagation that allows to describe the position of the wave ray in the horizontal plane. Considering the evolution of this reflection angle for waves that repeatedly reflect off an inclined slope, a new trapping mechanism emerges that displays the tendency to align this angle with the upslope gradient.

In the rather simple geometry of a translationally invariant canal, we show first that this configuration leads to trapezium-shaped attractors, very similar to what has been extensively studied in two-dimensions. However, we also establish a direct link between the trapping and the existence of two-dimensional attractors.

In a second stage, considering a geometry that is not translationally invariant, closer to realistic configurations, we prove that although there are no two-dimensional attractors, one can find a structure in three-dimensional space with properties similar to internal wave attractors: a one-dimensional attracting manifold. Moreover, as this structure is unique, it should be easy to visualize in laboratory experiments since energy injected in the domain would eventually be confined to a very thin region in three-dimensional space, for which reason it is called a super-attractor.

© 2019 Published by Elsevier Masson SAS.

Contents

1. Introduction

The unusual properties of internal waves propagating in stratified fluids lead to a particularly interesting phenomenon that has been studied in several situations in two dimensions: the existence of internal wave attractors. The latter correspond to a limit cycle towards which internal waves will focus in most confined geometries with at least one sloping boundary. These beautiful mathematical patterns exist thanks to the very peculiar non-specular reflection law that linear internal gravity waves obey. Nonlinearity is effectively introduced by the dynamical system that repeated application of this reflection law entails.

The large majority of internal wave attractor studies were restricted to two-dimensional geometries [1]. Despite their intriguing properties at the origin of many very interesting works, if one wants to study their possible oceanographic and astrophysical relevance, one has to consider three-dimensional situations. This is the main goal of this paper, in which we will use ray tracing to study the most interesting situations.

In the literature, wave attractor studies set in three dimensions were mostly restricted to spherical shells [2] that are particularly relevant in astrophysics [3]. Indeed, it is usual to consider the interior of gaseous planets as a fluid, (at least partially) stratified radially, around a solid or very dense liquid core [4]. Internal waves propagating within this spherical shell may indeed strongly influence the dynamics of the planet [5]. With a view of modeling internal tides in a channel, their three-dimensional behavior was also investigated numerically in a rotating, uniformly-stratified parabolic channel [6]. Taking into account the strong analogy between inertial and internal waves, one can also refer to works that considered rotating fluids in spherical [7], or trapezoidal [8] basins.

Using three dimensional ray tracing algorithms in these geometries, these authors were able to show that wave attractors obtained in two dimensions were not affected by the third dimension. They just keep their two-dimensionality. Owing to a residual symmetry, such as an invariance to translation (due to along-slope uniformity) or rotation (cylindrical or spherical symmetry), a *set* of attractors may exist side-by-side. Together they can be seen as a two-dimensional attracting manifold.

One may however ask two important questions:

(i) What are the conditions for the existence of two-dimensional attracting manifolds when considering general three-dimensional geometries?
(ii) Is it possible for basin geometries in which residual symmetries are absent to exhibit one-dimensional attracting manifolds, not contained in a plane?

These are the two objectives of this paper. In Section 2, we first present the propagation of internal wave beams before focusing on the reflection in three dimensions. We derive the reflection law for internal waves reflecting off an inclined slope and, using dynamical systems theory, we discuss in detail the map linking a wave beam's incident angle relative to the direction of the bottom gradient to its

reflected angle. In Section 3, we exhibit two-dimensional attractors in three dimensions before considering, for the first time in Section 4, a fully tridimensional geometry with 'super-attractors'. Finally, in Section 5, we conclude and draw some perspectives.

2. Propagation and reflection in three dimensions

2.1. Three-dimensional propagation

In an inviscid and incompressible fluid, linearly stratified along the vertical z-axis, internal waves correspond to perturbations of the velocity, the pressure and the density fields

$$\vec{V} = \vec{V_0} + \vec{v}, \quad P = P_0 + p, \quad \varrho = \bar{\rho}(z) + \rho'(x, y, z, t) \quad (2.1)$$

in which $\bar{\rho}(z)$ is the unperturbed linear stratification and with $|v| \ll |V|, |p| \ll P_0$ and $|\rho'| \ll \rho_0$.

In the framework of the Boussinesq approximation with $\rho_0 = \langle \bar{\rho} \rangle$ the average density over the stratified region, the projections of the Navier–Stokes equation on the three axes lead in the linear regime to

$$\frac{\partial \vec{v}}{\partial t} = -\frac{1}{\rho_0} \vec{\nabla} p + b \, \vec{e_z} \quad (2.2)$$

where buoyancy $b \equiv -\rho' g / \rho_0$, while the conservation of buoyancy reads

$$\frac{\partial b}{\partial t} + w N^2 = 0. \quad (2.3)$$

Here we introduced the square of the buoyancy frequency $N^2 = -(g/\rho_0)\mathrm{d}\bar{\rho}/\mathrm{d}z$, assumed to be constant. Combining appropriately Eqs. (2.2) and (2.3) and their time or spatial derivatives, one finally gets using the incompressibility condition

$$\frac{\partial^2}{\partial t^2} \nabla^2 v_z + N^2 \left(\frac{\partial^2}{\partial x^2} + \frac{\partial^2}{\partial y^2} \right) v_z = 0. \quad (2.4)$$

Plane waves $v_z = v_{z0} \exp(i(\omega t - \vec{k}.\vec{x}))$ with wavevector $\vec{k} = (k_x, k_y, k_z)$ and frequency ω, are solutions provided that the dispersion relation

$$\omega = \pm N \sqrt{\frac{k_x^2 + k_y^2}{k_x^2 + k_y^2 + k_z^2}} \quad (2.5)$$

is satisfied. Plane internal waves of frequency ω propagate their energy along the direction of the group velocity vector. Let us denote such an internal wave beam a 'ray'. Calling θ the angle of the ray with respect to the horizontal, one thus recovers in this three-dimensional setting $\omega = \pm N \sin \theta$ that requires that plane waves with frequency ω are propagating with a given and constant angle θ with the horizontal. In three dimensions, internal wave rays of fixed frequency therefore lie on a double cone. As the current velocity vector associated with such an internal wave is parallel to the rays, these also lie on the same double cone

$$v_z = \pm \tan \theta \sqrt{v_x^2 + v_y^2} \quad (2.6)$$
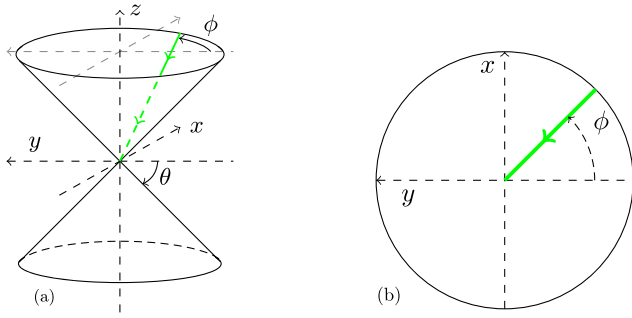
Fig. 1. Double cone with aperture $\pi/2 - \theta$ representing all possible propagating rays with frequency $\omega = \pm N \sin\theta$. Either half of the double cone on one side of the apex is called a cone. Drawn in green, a ray is characterized by its horizontal angle ϕ. Perspective view (a) and top view (b). (For interpretation of the references to color in all figure legends, the reader is referred to the web version of this article.)

represented in Fig. 1(a) and that reduces to the St Andrew's cross in two dimensions. The propagation of an internal wave ray with frequency ω is thus described by its position (x, y, z) and two angles: the horizontal propagation angle ϕ with respect to the downslope-directed y-axis and the angle θ that is linked to its vertical inclination.

It is important to realize that these five parameters (v_x, v_y, v_z, θ, ϕ) are not strictly equivalent to the three components of the position and of the velocity given usually for describing the motion of an object. However, as we will show below, due to focusing/defocusing of the wave component propagating in bottom-normal direction this norm is not conserved upon reflection of an internal wave off an inclined slope. During focusing it amplifies which increases our interest in its location. When a ray approaches an attractor, the ray path tells us where we should be looking because all the internal wave energy goes to that location. Therefore, for now the main interest of this paper is in the direction of the ray, not the wave field's magnitude.

For any θ-value, by stretching or compressing the z-axis with a factor $\tan\theta$, it is possible to map the problem to the value $\theta = 45°$ that we will assume for the remainder of the paper. In this case, the three components of the velocity field of an internal wave ray characterized by the horizontal angle ϕ are $(v_x, v_y, v_z) = (v_z \sin\phi, -v_z \cos\phi, v_z)$, that leads precisely to the equality $v_z^2 = v_x^2 + v_y^2$.

2.2. Reflection off an inclined plane

The impermeability condition when internal waves reflect from a plane, $z = sy$ inclined with an angle α with respect to the horizontal $y-$direction and having slope $s = \tan\alpha$ implies that the normal group velocity should vanish at the boundary, while the inviscid hypothesis and the invariance along the x-direction leads to the conservation of the along slope group velocity. Taking into account the incident (denoted with the index i) and reflected (denoted with the index r) particle velocity $\vec{v}_i \exp[i(\omega_i t - \vec{k}_i \cdot \vec{r})] + \vec{v}_r \exp[i(\omega_r t - \vec{k}_r \cdot \vec{r})]$, the above condition first implies that the frequency ω is kept constant. Introducing the incident $\vec{v}_i = (v_{x,i}, v_{y,i}, v_{z,i})$ and the reflected $\vec{v}_r = (v_{x,r}, v_{y,r}, v_{z,r})$ velocity fields, these remarks can be summarized in the following three conditions for reflection:

(a) $\theta_r = \pm\theta_i \mod \pi$ the reflected and incident waves are on the same double cone.
(b) $v_{x,r} = v_{x,i}$ the along-slope component is unchanged.
(c) The component of the velocity normal to the slope changes its sign, that leads to

$$v_{z,r} \cos\alpha - v_{y,r} \sin\alpha = -(v_{z,i} \cos\alpha - v_{y,i} \sin\alpha) \tag{2.7}$$

that can be simplified using $s = \tan\alpha$ as

$$v_{z,r} + v_{z,i} = s(v_{y,r} + v_{y,i}). \tag{2.8}$$

Condition (a) taking into account Eq. (2.6) with $\theta = 45°$ leads directly to $v_{z,r}^2 = v_{x,r}^2 + v_{y,r}^2$ and $v_{z,i}^2 = v_{x,i}^2 + v_{y,i}^2$. Subtracting both equalities and using condition (b), one gets

$$(v_{z,r} - v_{z,i})(v_{z,r} + v_{z,i}) = (v_{y,r} - v_{y,i})(v_{y,r} + v_{y,i}). \tag{2.9}$$

For a sloping boundary, $(v_{y,r} + v_{y,i})$ is non-zero. Hence, by combining Eqs. (2.8) and (2.9) this term can be divided out, which leads to the following system of two equations with two unknowns $v_{z,r}$ and $v_{y,r}$:

$$v_{z,r} + v_{z,i} = s(v_{y,r} + v_{y,i}), \tag{2.10}$$
$$v_{y,r} - v_{y,i} = s(v_{z,r} - v_{z,i}). \tag{2.11}$$

Recalling condition (b) for the along-slope velocity component, the above system leads to

$$v_{x,r} = v_{x,i}, \tag{2.12}$$
$$v_{y,r} = \frac{(1 + s^2)v_{y,i} - 2sv_{z,i}}{1 - s^2}, \tag{2.13}$$
$$v_{z,r} = \frac{-(1 + s^2)v_{z,i} + 2sv_{y,i}}{1 - s^2}, \tag{2.14}$$

providing the reflected ray from the knowledge of the incident one.

It is interesting to derive the corresponding law between the incident and reflected horizontal angles ϕ_i and ϕ_r, both angles being defined in Fig. 2. Recalling that $v_x = v_z \sin\phi$ and $v_y = -v_z \cos\phi$, the ratio of Eqs. (2.12) and (2.14)

$$\frac{v_{x,r}}{v_{z,r}} = \sin\phi_r = \frac{(s^2 - 1)\sin\phi_i}{1 + s^2 + 2s \cos\phi_i}, \tag{2.15}$$

which can be written as a map defining the subsequent angle of incidence, $\phi_i' \equiv \pi + \phi_r = \mathcal{R}(\phi_i, s)$, detailed in Appendix. Above formula was originally derived by Maas [1]. Interestingly, one can easily check that this law is also valid when considering horizontal ($s = 0$) or vertical ($s \to \infty$) boundaries.

Note that in the remainder of the paper, this transformation will always be associated with an appropriate normalization of the reflected velocity field. Indeed, as in two dimensions, the norm of the velocity field is not a conserved quantity through the reflection mechanism. Consequently, such a normalization is natural to avoid any numerical difficulties, especially as our primary interest is the direction of the velocity vector rather than its magnitude.

## 2.3. Study of the reflection map $\mathcal{R}$

In order to understand the variation of the angle because of the reflection, instead of studying the reflected angle ϕ_r itself, it is more appropriate to consider ϕ_i', the following incident angle once the ray will come back towards the slope upon an intermediate surface reflection, analogously to a Poincaré map. Indeed, after reflection the green ray represented in Fig. 2 is transformed into the red one that will encounter horizontal or vertical walls, before coming back towards the slope of interest, with an angle $\phi_i' = \pi + \phi_r$ as shown by the green dashed ray in the example of Fig. 2b. An example of such a possible trajectory is depicted in Fig. 3(a).

This is of course not the general situation since the ray can impinge on a vertical wall and then on an horizontal one, before coming back towards the slope with an angle $\phi_i' = -\phi_r$. However, let us discuss first a simple case that will allow us to derive global and rather generic properties of this reflection law.

Once the angle of the slope is given, the value of s is known and then one can study the map $\mathcal{R}$ providing ϕ_i' as a function of ϕ_i (see Appendix for useful detail). Note that for $s = \tan\alpha < 1$, only the
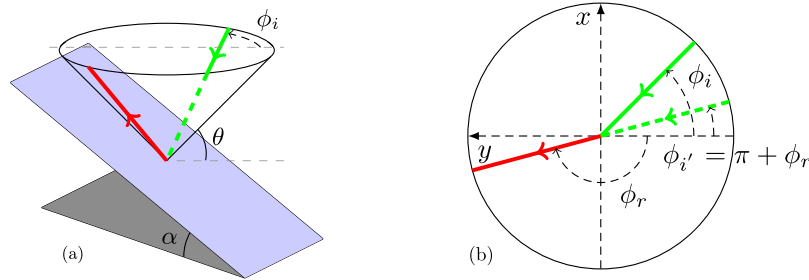
Fig. 2. Perspective view (a) and top view (b) of the reflection of an internal wave beam off an inclined slope. The bottom, inclined at angle α with respect to the horizontal xy-plane, is represented by the inclined blue rectangle. The internal wave beam propagates along a cone whose inclination, θ, is set by the ratio of wave and buoyancy frequencies. The incident (in green) and reflected (in red) beams make angles $\phi_i > 0$ and $\phi_r < 0$ relative to the downslope direction, respectively. The green dashed line is discussed in the text.
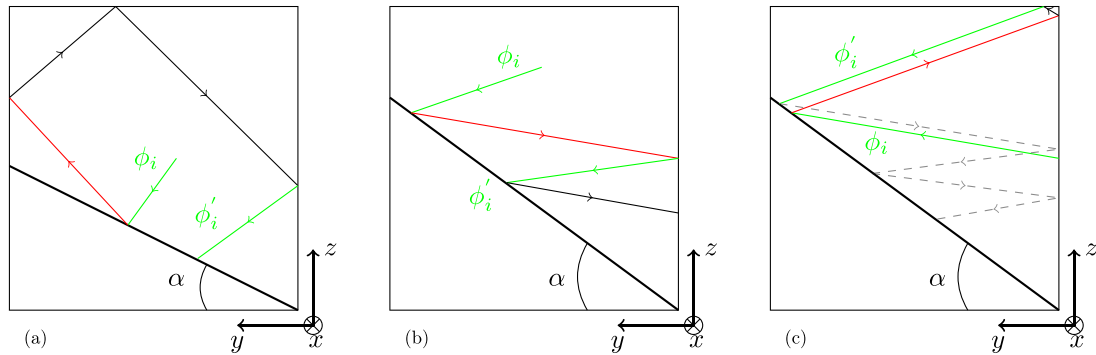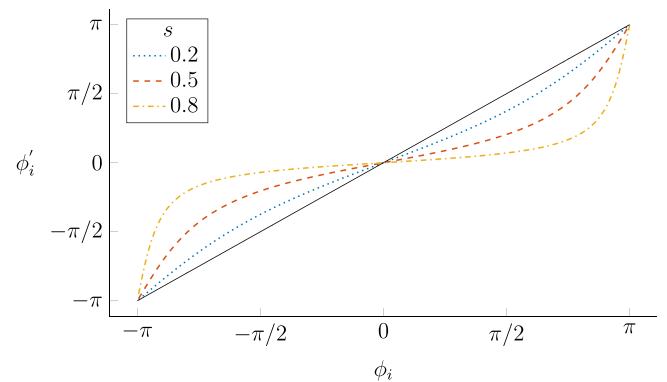

Fig. 3. Possible reflections of an internal wave off a bottom whose slope is subcritical (left panel) or supercritical (center and right panels). In the right panel, the trajectory is represented with a dotted line after the second reflection. Next to each ray, the corresponding horizontal angle ϕ is written. Note that this picture, being a side view displays only the projection of horizontal angles ϕ on the yz plane.

top cone of Fig. 1 is physically interesting since the bottom one is fully below the slope.

Let us study separately the three different cases: $s < 1$, $s = 1$ and $s > 1$.

2.3.1. Subcritical reflections $s < 1$

Fig. 4 presents the evolution of the angle ϕ_i' as a function of ϕ_i, for different subcritical cases with $s < 1$. One realizes immediately that for any s-value, the function intersects the diagonal line in $\phi_i = 0$ and $\pm\pi$. There are therefore three fixed points of map $\mathcal{R}$ (actually two since $\pm\pi$ correspond to the same physical state). For any value $s < 1$, as $\mathcal{R}'(0) < 1$ while $\mathcal{R}'(\pm\pi) > 1$, only $\phi^\star = 0$ is a stable fixed point, corresponding to upslope propagation. The reflection off the inclined slope of an internal wave ray has therefore the systematic tendency to reduce its horizontal angle. This is what we will call in the remainder of the paper, the trapping effect. Fig. 4 shows that the closer the value of s is to 1, the faster is the trapping effect.

2.3.2. Critical reflection $s = 1$

In the theoretical case $s = 1$, the angle of the slope coincides with the aperture of the double cone. Eqs. (2.13) and (2.14) show that, in that case, $v_{y,r}$ and $v_{z,r}$ diverge. Eq. (2.15) is however still valid and leads to $\phi_i' = 0$ for any initial horizontal angle ϕ_i. The trapping is total from the very first reflection.

2.3.3. Supercritical reflection $s > 1$

Fig. 5 shows that in that case the top cone is not anymore fully attainable. Introducing the limiting angle $\phi_\ell = \arctan\sqrt{s^2 - 1}$, one realizes that ϕ_i has to be restricted to $[-\pi + \phi_\ell, \pi - \phi_\ell]$ for the top cone and to $[-\phi_\ell, \phi_\ell]$ for the bottom one. Fig. 6 presents the analysis for reflections on the top ($v_{z,i} < 0$) and the bottom ($v_{z,i} > 0$) cones, that have to be studied separately.

Fig. 4. Map $\phi_i' = \mathcal{R}(\phi_i, s)$ for $\phi_i \in [-\pi, \pi]$ for three different values of $s < 1$. The solid diagonal line represents $\phi_i' = \phi_i$.

(i) For rays impinging on the top cone, $\phi_i \in [-\pi + \phi_\ell, \pi - \phi_\ell]$, one gets $v_{z,r} < 0$, implying that the reflected ray belongs (and is restricted) to the bottom cone.

Reflections on vertical or horizontal boundaries leading to $\phi_i' = \pi + \phi_r$, like in Fig. 3(a), are therefore not possible. On the contrary, the situation is like the one presented in Fig. 3(b), in which the wave reflects on a vertical boundary before coming back towards the slope, leading to $\phi_i' = -\phi_r$ shown in Fig. 6. Here again, there is one unique stable fixed point, that is $\phi^\star = 0$. One finds once more that the three-dimensional reflection law has the tendency to straighten the horizontal angle of propagation. However, this case is of limited consequences; indeed, in the canal geometry that we will be interested in, when $s > 1$, the two-dimensional version leads to a point
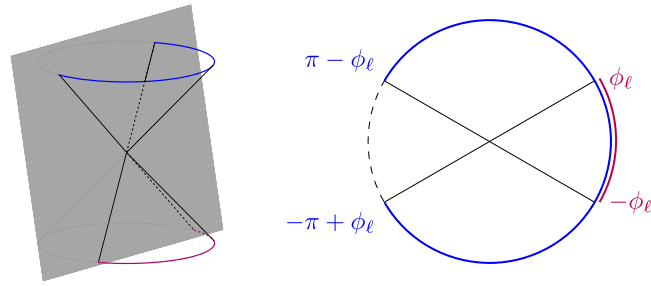
Fig. 5. Cone of possibilities for a *super*critically sloping bottom $s > 1$. The left panel shows that the planar slope, in gray, inclined with an angle α, partially intersects the double cone. The right panel presents the available angular sector for ϕ_i on the top (resp. bottom) cone in blue (resp. mauve).
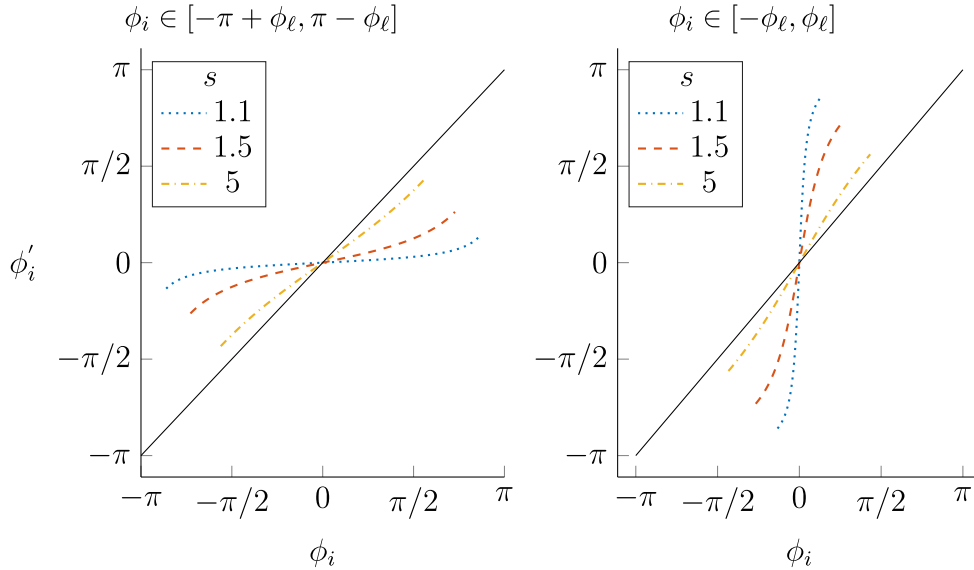
Fig. 6. Map $\phi_i' = \mathcal{R}(\phi_i, s)$ for three different values of $s > 1$ for an internal wave ray impinging on the top cone (left panel with $v_{z,i} = -1$) and on the bottom one (right panel with $v_{z,i} = 1$). The solid diagonal line represents $\phi_i' = \phi_i$.
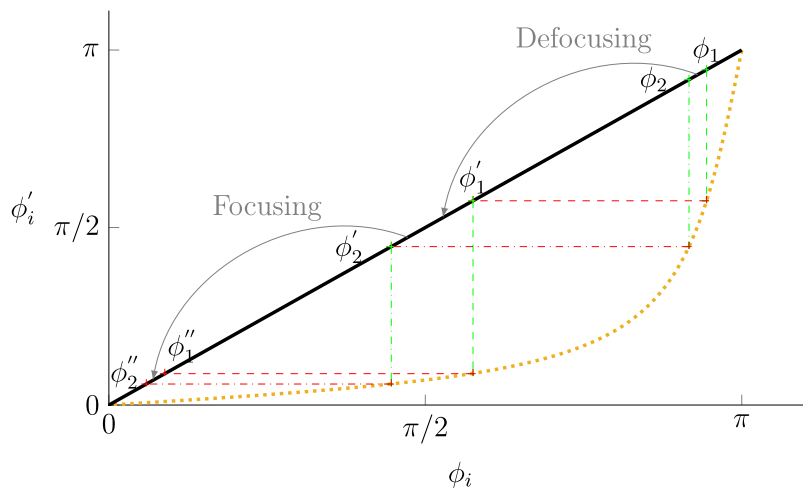

Fig. 7. Map $\phi_i' = \mathcal{R}(\phi_i, s)$ for $\phi_i \in [0, \pi]$ for $s = 0.8$ represented with the yellow dotted line. We follow two different reflections (dash-dotted and dashed lines) initiated from two initial horizontal angles ϕ_1 and ϕ_2. As previously, green (resp. red) corresponds to incident (resp. reflected) rays. The diagonal line $\phi_i' = \phi_i$ is represented by the solid black line.

attractor, with all wave rays ending in the bottom right corner as one can guess by looking at Fig. 3(c).

(ii) For incident wave rays on the bottom cone, $\phi_i \in [-\phi_\ell, \phi_\ell]$ that leads to $v_{z,r} > 0$: the reflected ray is therefore on the top cone. Not unexpectedly, this case corresponds precisely to the previous one, once the sense of propagation has been

reversed. After a series of reflections as plotted in Fig. 3(c), one finds the reflection law $\mathcal{R}$ detailed in Appendix for $v_{z,i} > 0$ (see right panel of Fig. 6). This time, the reflection is defocusing since $|\phi_i'| > |\phi_i|$ for any value $s > 1$: the fixed point 0 is thus unstable. However, as shown by the example depicted in Fig. 3(c), one will not indefinitely get reflections with $v_{z,i} >$
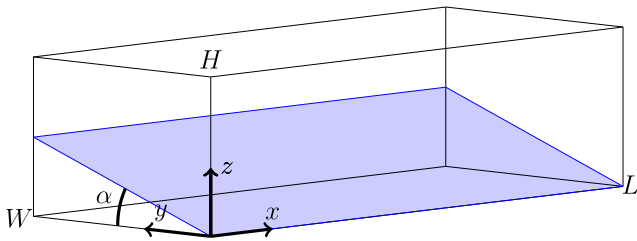
Fig. 8. Geometry under investigation with the definition of the height H, length L and width W of the canal. The slope, inclined at the angle α with respect to the horizontal xy-plane, is represented by the blue rectangle.

0 since, eventually, due to a reflection at the horizontal rigid-lid surface one will get $v_{z,i} < 0$, corresponding to the previous case.

Moreover, if the upper boundary of the domain (the surface in the present case) is high enough, as the function is an increasing function of its argument, one eventually reaches a value ϕ_i' that will be greater than ϕ_ℓ. Above that value, one cannot have anymore reflection with $v_z > 0$, and one comes back to the previous case converging towards the fixed point $\phi^\star = 0$.

In summary, in the situations that we have considered, the ray is eventually trapped in the plane corresponding to a vanishing horizontal angle ϕ. This is the generic case, but as we will discuss below, trapping may not occur in some peculiar cases.

2.3.4. Focusing or trapping?

We called *trapping* the alignment of the horizontal angle ϕ with respect to the downslope direction of the reflecting slope. It is important to distinguish this from the focusing that occurs in two-dimensions, when a corresponding internal wave beam reflects off a slope. Focusing corresponds to the decrease of the width of the beam after reflection, or alternatively, to the decrease of the distance between two rays initially parallel and impinging on a planar slope.

In three dimensions, the analog of this focusing would correspond to a study of the angular gap $\phi_2 - \phi_1$ between both rays. In a situation where trapping is present as shown in Fig. 7 for $s = 0.8$, one sees that the reflection off an inclined slope could be focusing or defocusing. The gap between two initial angles increases after the first reflection, before decreasing. The first reflection is therefore defocusing, while the second is focusing. On the contrary, both reflections lead to smaller values of the angle, they are trapping. Trapping and focusing are corresponding therefore to different ideas. Defocusing occurs between two rays characterized by ϕ_1 and ϕ_2 if and only if $\mathcal{R}'(\phi) > 1$ for $\phi \in [\phi_1, \phi_2]$, where a prime indicates a derivative to its argument. Reciprocally, focusing occurs when $\mathcal{R}'(\phi) < 1$ in this interval.

3. 2D attractors in a 3D geometry

3.1. Choice of the geometry

Having presented the trapping mechanism due to the reflection off a slope, let us turn to its consequences in a canal with an inclined slope as depicted schematically in Fig. 8. This geometry, that we used to derive the reflection law (2.15), has several advantages:

(i) Corresponding to a schematic simplification of estuaries or river arms, it has *a geophysical interest*. The Lower St. Lawrence Estuary (Eastern Canada) with its river bed essentially U-shaped transversally and longitudinally invariant

over 1000 km [9] is a prototypic example. This site is remarkable since even though internal tides are known to be generated at the land-locked head of the Channel [10], surprisingly low intensity internal tides have been measured near the mouth of the Laurentian Channel, eastern Canada [11]. It is therefore important to study propagation and reflection of internal waves in such a geometry.

(ii) This geometry is *simple and easy to implement experimentally*, before studying in a second stage more complicated ones.

(iii) *A theoretical interest* can also be anticipated from this geometry from the study presented in the preceding section. Indeed, when an internal wave ray reflects off a subcritical slope (as sketched in Fig. 3(a)), there is one single fixed point of the iterated map, $\phi^\star = 0$, that proves that the ray will eventually converge to a yz-plane, transverse to the canal. The internal wave will therefore be trapped.

Interestingly, the transversal cut of the canal is precisely the appropriate geometry leading, in two dimensions, to internal wave attractors. In a given geometry, an internal wave attractor is a path towards which all internal waves of a given frequency will converge: the existence of such a limit cycle has been tested through ray tracing and experiments in various geometries [1,12–15], and has been confirmed in an exceptional case analytically [16]. Depending on a dimensionless lumped parameter containing the aspect ratio and the ratio of wave to buoyancy frequencies, for the same geometrical domain, different attractors exist; they are labeled using two indices (m, n), in which m and n describe the number of reflections on a vertical wall and on the slope respectively.

3.2. Simple attractors

Let us consider first the simplest case for which the transverse geometry (i.e. in the yz-plane) leads to $(1,1)$ attractors. We will moreover consider the subcritical case $s < 1$. As the successive reflections will occur with an incident horizontal angle ϕ_i between 0 and π, the right panel of Fig. 4 shows that the angle will converge towards the fixed point $\phi^\star = 0$. This is indeed possible since the $(1,1)$ attractor loop allows $\phi_i' = \pi + \phi_r$, as shown by Fig. 3(a).

The important parameters for ray tracing are:

- Geometrical ones (H, W, α). Note that the dimensionless length of the canal is $L = 1000$.
- The angle of propagation of internal waves θ has been chosen to lead to a $(1,1)$ attractor. It is not useless to recall that, in the ray tracing, θ is always equal to $\pi/4$ by modifying the height H with the factor $\tan\theta$ that stretches the vertical.
- The initial values of the ray (x_0, y_0, z_0, ϕ_0) and v_{z0} that determines the sheet of the double cone that is initially chosen.

A typical trajectory is plotted in Fig. 9 with different views. It is clear that the ray, initially launched in the longitudinal x-direction, after a finite number of reflections on the sloping bottom, eventually rotates towards a transverse plane. Fig. 9(c) reveals that the transverse structure of the trajectory is an attractor, identical to those obtained in 2D [1,12,13]. Note however a fundamental difference with respect to the 2D propagation: the rays do no longer propagate only along one of the four different angles $\theta, -\theta, \pi - \theta, \pi + \theta$, but involve a horizontal angle of propagation, ϕ, too. Fig. 9(c) shows only the angle projected on the transverse plane; it coincides precisely with one of these four possibilities only if $\phi = 0$, which indeed is reached asymptotically.

The above discussion has emphasized how the trapping mechanism occurs in three dimensions, and transforms an initial longitudinal propagation into an attractor in the transverse plane. We will turn towards the trapping and the convergence times, two important notions.
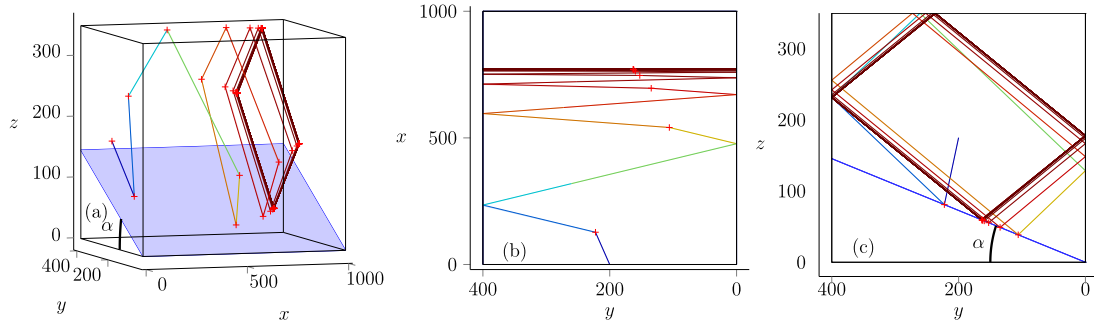
Fig. 9. Perspective (a), top (b) and side (c) views of the trajectory of a single internal wave beam propagating in the canal-like geometry filled with a linearly stratified fluid and the following geometrical parameters: $H = 350, W = 400, L = 1000, \alpha = 20°$ and $\theta = 35°$. The beam is sent downwards (in the negative z-direction) from the plane $x = 0$ with $y_0 = W/2$ and $\phi_0 \simeq \pi/2$ (i.e. into the positive along-tank x-direction). Panel (b) shows the convergence of the horizontal angle ϕ towards $\phi^\star = 0$, (rebounds on the slope are indicated with red crosses), while panel (c) emphasizes the limit cycle of the (1,1) attractor. The color of the ray progressively changes from blue to red with the advancement of the ray.
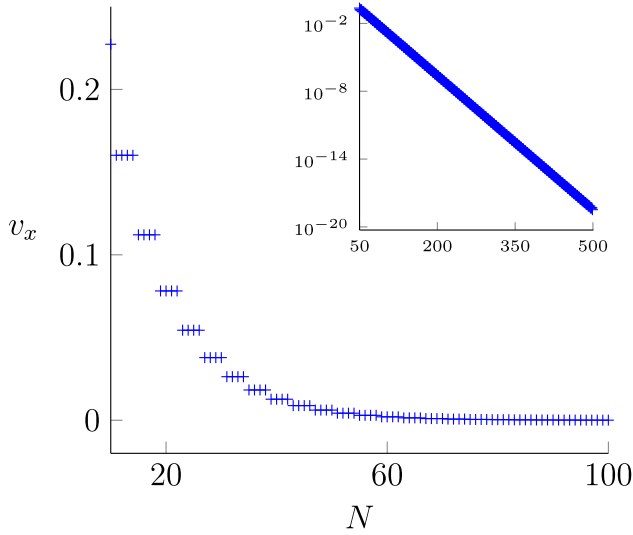
Fig. 10. Evolution of the longitudinal velocity component v_x in linear scale as a function of the number of reflections. The inset presents the same plot in semilogarithmic scales. For this plot $\alpha = 8°$ and therefore $s = 0.18$.

3.2.1. The trapping time

The speed of convergence of the trapping is not always as progressive as the example shown in Fig. 9 for which, in order to identify the different regimes, parameters have been tuned to get a trapping, neither too fast, nor too slow.

Instead of considering the evolution of the angle ϕ as a function of the number of reflections, one can study the longitudinal velocity component v_x. As briefly discussed in Section 2.2, because of the specifics of this reflection process, the longitudinal component v_x stays constant while both transverse ones, v_y and v_z, diverge towards infinity. To avoid this divergence, the total velocity has therefore been normalized after each reflection. During the trapping, one thus gets $v_z \to \pm 1/\sqrt{2}$ and $v_y \to \mp 1/\sqrt{2}$ while $v_x \to 0$, the signs between v_y and v_z being exchanged at each reflection.

Fig. 10 presents the longitudinal component v_x as a function of the number of reflections on boundaries. The rebounds on the horizontal or vertical boundaries do not modify v_x. On the contrary, it strongly decreases when the reflection occurs on the slope. In agreement with the geometrical structure of the (1,1) attractor with three non-focusing vertical or horizontal sides and only one slope, this is the reason for the four identical values before a drop corresponding to a reflection off the inclined slope.

To characterize the velocity of trapping that Fig. 10 suggests to be exponential, let us introduce the coefficient γ_p defined as

the ratio between the horizontal velocity components before the reflection, v_x, and after, v'_x. Since the horizontal component is modified only by the normalization, one gets

$$\gamma_p = \left(v_x'^2 + v_y'^2 + v_z'^2 \right)^{-1/2} \tag{3.1}$$

$$= \left(v_x^2 + \frac{1}{(1-s^2)^2} \left[(v_y^2 + v_z^2)((1+s^2)^2 + 4s^2) \right. \right.$$

$$\left. \left. -8sv_yv_z(1+s^2) \right] \right)^{-1/2}. \tag{3.2}$$

In order to get rid of the dependence of this coefficient with respect to the components of the velocity, it is necessary to consider the regime close to the convergence towards the fixed point. As discussed in previous section, in this regime, the horizontal component v_x can be neglected with respect to v_y and v_z. Taking advantage of the normalization, one gets $v_y^2 + v_z^2 \approx 1$ and $v_yv_z = -1/2$, that leads to

$$\gamma_p \simeq \left(0 + \frac{[(1+s^2)^2 + 4s^2 + 4s(1+s^2)]}{(1-s^2)^2} \right)^{-1/2} \tag{3.3}$$

$$= \frac{1-s^2}{(1 + 4s + 6s^2 + 4s^3 + s^4)^{1/2}} \tag{3.4}$$

$$= \frac{1-s}{1+s}, \tag{3.5}$$

the focusing power of normally-incident internal waves reflecting off an inclined wall of slope s. In the framework of this approximation, the convergence is therefore exponential with the number N of reflections since one can write $v_x(N) = v_x(0)\gamma_p^N = v_x(0)e^{N\ln\gamma_p}$. It is straightforward to check that γ_p is less than 1; it is also a decreasing function with the gradient of the slope, s, and tends towards zero as s tends toward unity (we recall that this discussion is performed in the subcritical regime).

The example presented in Fig. 10 attests that this approximation is very quickly valid. The inset of the exponential relaxation leads to $\ln \gamma_p^{num} \simeq -0.091$ that one can compare to the predicted value. Once the value $s = \tan\alpha/\tan\theta = 0.178$ is obtained from the angle of the slope $\alpha = 8°$, one just has to realize that only the reflection on the slope is effectively trapping, while the three successive reflections on the vertical or horizontal boundaries are not modifying the velocity components. Once this factor four is taken into account, one gets $\ln \gamma_p^{th} \simeq -0.090$ that does confirm the approach.

3.2.2. The convergence time

It is important to make a distinction between the trapping time, defined as the inverse of $\ln \gamma_p$, and the convergence time, that could

be defined as the time for the ray to be really trapped. Indeed, successive reflections on vertical and horizontal boundaries do not necessarily each lead to $\phi_i' = \pi + \phi_r < \phi_i$ as in the example in Fig. 3(a). Several untrapping reflections can follow one another, and consequently significantly delay the trapping.

Fig. 11 presents three examples, in which only the initial position y_0 has been modified, but leading to significantly different convergence times. Geometrical parameters used in the ray tracing presented in Fig. 9 have been kept constant, but only the value for α is now smaller to get a slower trapping, and the value θ has been modified to correspond again to a $(1,1)$ attractor.

These examples show that, due to reflections on the boundaries, the velocity component changes its sign several times, before the exponential trapping towards zero occurs, as discussed in Section 3.2.1 It is clearly apparent in these examples that the exponential decay lasts much less than the first phase of the evolution. The trapping time discussed earlier is therefore not always the appropriate quantity to characterize the convergence. The first regime can last a transitory but long time, before the ray falls into a funnel and becomes fully trapped.

In summary, despite a value of s being close to 1 that suggests a fast decay of the velocity component v_x, the trapping time may be very long, depending on the geometrical parameters and initial conditions. Such an effect will be central when dissipation will come into play. Indeed, a large number of reflections usually means a long distance of propagation and therefore a strong decay in amplitude when viscous effects cannot be neglected before any trapping can take place. In such cases, predictive aspects of ray dynamics become less meaningful.

3.2.3. Trapping plane

The longitudinal coordinate of the trapping yz-plane is clearly also an important quantity, especially for what concerns any tentative experimental application. To determine its coordinate that we will call x_∞, one has to study its dependence with the two launching coordinates y_0 and z_0. Taking advantage of the exponential relaxation, the criterion chosen is that the x-component of the velocity field is four orders of magnitude smaller than the two other components.

Fig. 12(a) and (b) show for different initial conditions, varying the coordinates (y_0, z_0) of the initial launching point (left panel) or of the initial horizontal angle ϕ_0 (right panel), the corresponding final paths. All rays converge towards the same structure, an attractor, but whose x-coordinate depends moderately on y_0 and z_0, but strongly on ϕ_0. By considering the limiting case, $\phi_0 = 0$, one indeed realizes that rays are restricted to the transverse plane and therefore in that case the trapping plane is $x_\infty = x_0$. The collection of attractors in these two panels illustrate the notion of an attracting two-dimensional manifold, existing due to along-slope translational symmetry.

Fig. 13 presents the position of the trapping plane x_∞ as a function of y_0 and z_0 in two cases: a beam propagating initially upward, $v_z = 1$ (left panel), or downward, $v_z = -1$ (right panel). The convergence of the first case $v_z = 1$ is in general slower since the first reflection on the sloping bottom is delayed with respect to the case $v_z = -1$. Other effects may come into play and modify the map. Indeed, discontinuities are due to reflection off the end wall of the canal-like geometry at $x = L$, that delays the trapping. These examples show the richness of this dynamical system and emphasize that, even in a case leading to a simple $(1,1)$ attractor, the convergence towards the trapping plane can be more complicated and with surprises.

3.3. More complicated attractors

3.3.1. Phase diagram

Considering cases not leading to the simple $(1,1)$ attractors, let us plot for the same geometry the diagram as a function of θ and α. The dimensions $H = 360$, $L = 1000$ and $W = 410$ are constant once the canal is given. While this diagram is not universal as the so-called (d, τ)-diagram reported for two-dimensional attractors in a trapezoidal domain by Maas [1] and discussed more recently in [17], we will show that it allows to vizualise the main regions with simple attractors.

Moreover, as discussed above, initial values for the launching point or the horizontal angle are generically not important since one gets eventually always the same attractor, only its position x_∞ changes. The phase diagram plotted in Fig. 14 shows on the left (resp. right) the number of reflections m (resp. n) of the final steady paths on the vertical wall $y = 0$ (resp. on the slope). They are plotted only for $\alpha < \arctan(H/W) \simeq 41°$, since for larger values the trapezoidal geometry is modified into a triangular domain in which all attractors boil down to a point attractor. Both pictures show to what kind of attractors the final steady paths belong to.

Let us describe the main areas in the diagram:

(i) The top right dark blue triangle corresponds to the convergence towards a domain without reflection, on the surface. It corresponds to the point attractors, that one precisely encounters in the supercritical regime $\alpha > \theta$ (see the central and right panel of Fig. 3 in which the ray eventually reaches the bottom right corner of the domain).

(ii) The blue tongues, present in both the right and left panels correspond to one reflection on the slope and one reflection on the vertical wall. These two pieces of information allows us to conclude the path is the one of a $(1,1)$ attractor. Panel (a) of Fig. 14 shows an example of such cases that we discussed in detail in previous sections.

(iii) Tongues that are only blue on the left panel (i.e. with one reflection on the vertical wall, $m = 1$) but differently colored (multiple reflections on the slope) on the right panel, correspond to $(1, n)$ attractors, with n given by the associated color of the tongue in panel (f). Panel (c) of Fig. 14 shows such an example corresponding to a $(1,3)$ attractor.

(iv) One can identify other structures in the phase diagrams in Fig. 14(b) and (d), and especially, colored tongues in both panels attesting more complex (m, n) attractors. One $(3,1)$ attractor (panel (b)) and one $(1,2)$ global resonance case (panel d), with 2 reflections from the slope, one focusing and one compensating defocusing reflection, which occupy a line in panels (e) and (f). Global resonances have n focusing reflections exactly compensated by n defocusing reflections. These are characterized by each ray being periodic, instead of, as for attracting cases, approaching a limit cycle.

(v) The remaining large domain in red, and therefore with $(m, n) > 10$, corresponds to even more complicated attractors. As for the (d, τ) diagram for two dimensional attractors in a trapezoidal domain, except for singular values (lines), one gets attractors for all (α, θ) values.

It is important to emphasize that there are no attractor regions with an even number of reflections N_s off the slope. This is a property already known for 2D attractors [1,15]. However, as briefly discussed, there exist lines at which $(m, 2n)$ global resonances can be found.

3.3.2. (1,3) attractor

Studying a $(1,3)$ attractor allows to better understand how trapping happens and when it cannot occurs. It is indeed known [1, 15] that $(1, 2n + 1)$ attractors have n defocusing reflections and
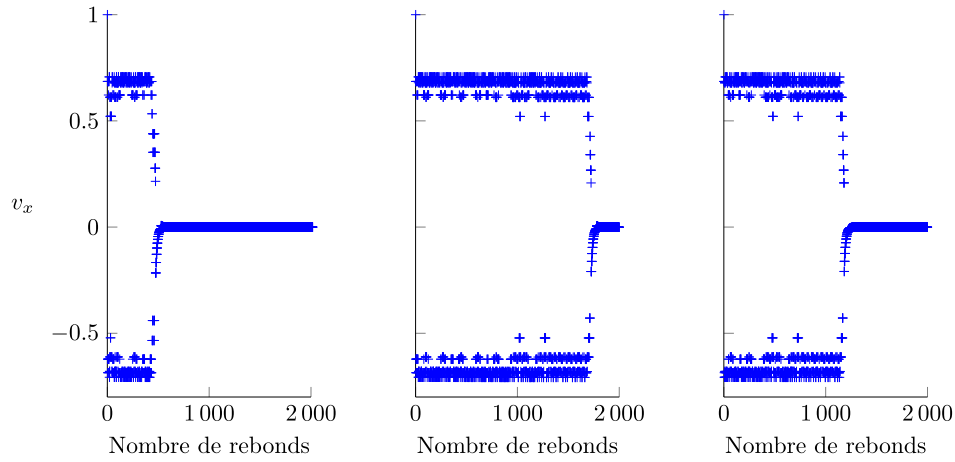
Fig. 11. Three examples for the evolution of the horizontal component v_x with $y_0 = 0.1W$ (left panel) $y_0 = 0.5W$ (center) $y_0 = 0.85W$ (right). Geometrical parameters are $H = 350$, $L = 1000$, $W = 400$, $\alpha = 6°$, $\theta = 38.3°$, $z_0 = 0.2H$, $x_0 = 0$ and $\phi_0 = 90°$.
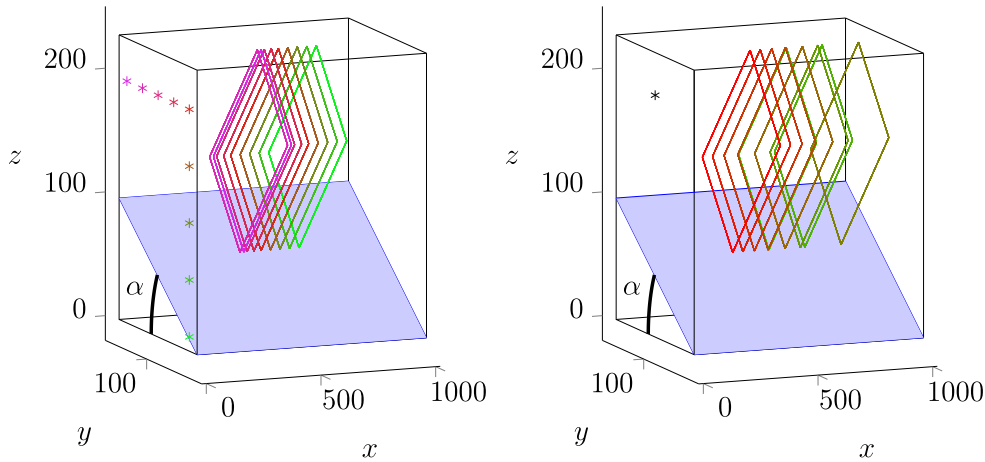

Fig. 12. The left panel shows final steady paths for different launching positions in the $x = 0$ plane. The initial launching point and the corresponding attractor are represented with the same color. ϕ_0 is always taken equal to $\pi/2$. The right panel presents results for the same initial launching point (black star) when spanning values of ϕ_0 between 20° (gray) and 90° (red).
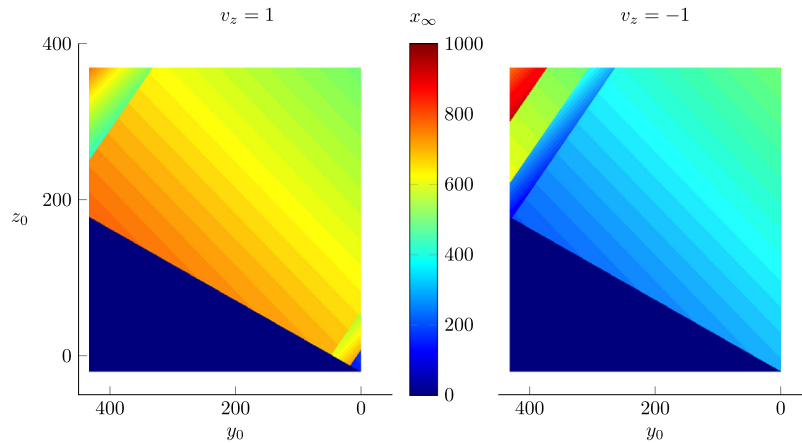

Fig. 13. Position x_∞ of the trapping plane for different initial conditions y_0 and z_0, while other parameters are kept constant, particularly $x_0 = 0$ and $\phi_0 = 47°$. The left (resp. right) panel corresponds to $v_z = 1$ (resp. $v_z = -1$). The blue triangle corresponds to the region below the slope.

$n + 1$ focusing ones. Indeed, in 2D, more *defocusing* than focusing reflections would mean that rays will on average move away from one another, which would lead to the absence of attractors.

A typical trajectory converging towards a $(1,3)$ attractor is plotted in Fig. 15. Reflections indexed by 1 and 3 are occurring along the gradient of the slope that leads to focusing. On the contrary,
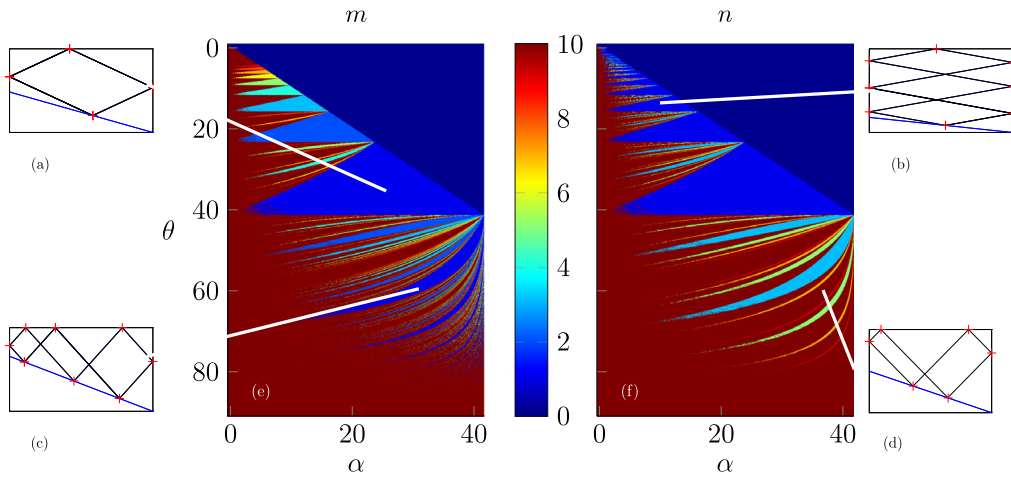
Fig. 14. Panel (e) and (f): phase diagrams of the steady paths as a function of the angles α and θ (in degrees), for the typical case $H = 360$ and $W = 410$, and $L = 1000$. Panel (e) and (f) give respectively the number of reflections off a vertical wall, m, and off the slope, n, using the central color table. The top-right triangles correspond to the point attractor zone, that exists in the subcritical case. Three different attractors are shown in panel (a), (b) (c) and a global resonance in panel (d), with a link to their region of existence indicated by the white segments.
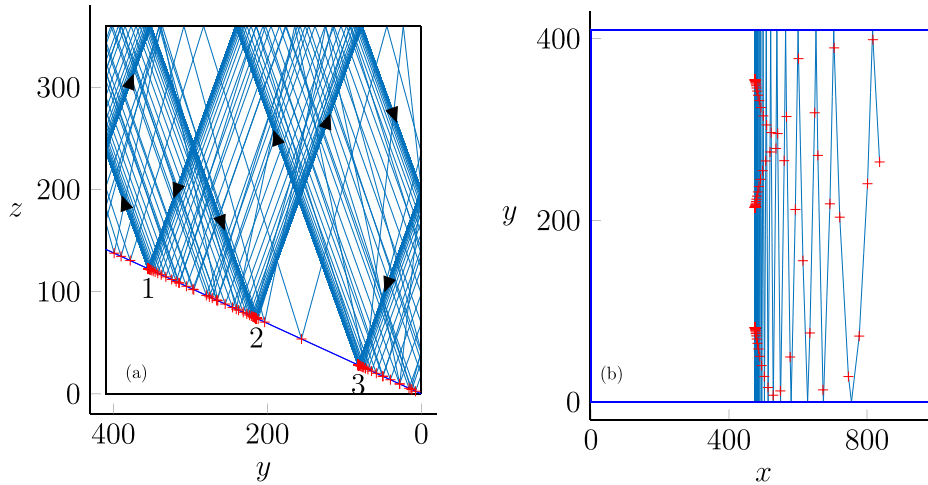
Fig. 15. Side (a) and top (b) views of a three-dimensional ray tracing in a geometry leading to (1,3) attractor. The corresponding transverse geometry leads to the same (1,3) attractor. Red crosses locate the reflections on the slope. Note that for the sake of clarity, the beginning of the ray tracing, initiated from $x = 0$ and bouncing back from $x = L$, has not been plotted. Numbers written just below the slope in (a) indexed the different reflections along the attractor.
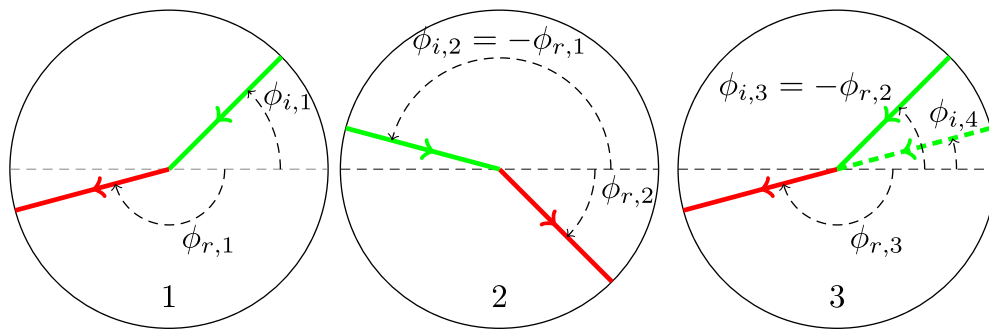

Fig. 16. Successive reflections on the slope for the trajectory of the (1,3) attractor presented in Fig. 15. Incident (resp. reflected) rays are plotted in green (resp. red).

reflection 2, being in the opposite direction of the gradient, is defocusing.

In the following, we will consider that the ray still not trapped has a path quasi identical to the one of a two-dimensional (1,3) attractor. Such an approximation is fully justified by the top view shown in the right panel of Fig. 15. After just a few rebounds, one can identify three reflections (identified by the red crosses) on

the sloping bottom. Their positions slightly change, but not their focusing or defocusing nature.

What can we say for the trapping in such a case? One cannot refer to the discussion of Fig. 4, in which all reflections led to trapping since, here, reflections on vertical and horizontal walls do not always give $\phi'_i = \phi_r$.
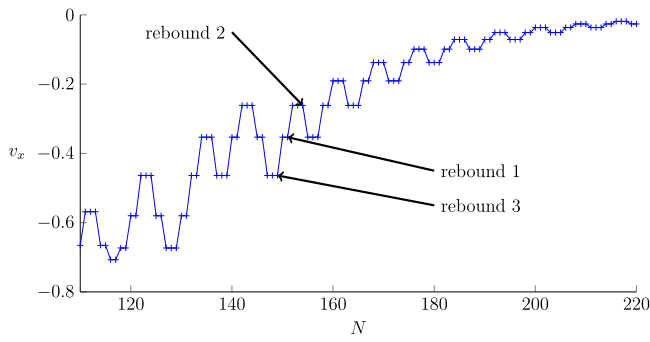
Fig. 17. Normalized velocity component v_x as a function of N the number of reflections for the trajectory depicted in Fig. 15. Two successive rebounds, 1 and 3, lead to a decrease of v_x in absolute value while, on the contrary, rebound 2 leads to an increase of v_x in absolute value unlabeled reflections from horizontal surface and vertical wall do not alter v_x.

Fig. 16 presents the projection of the ray in the xy-plane in the case with three reflections of the (1,3) attractor shown in Fig. 15. Panels (a), (b) and (c) present respectively the reflection numbered 1, 2 and 3. Because of the path of the (1,3) attractor, the reflected ray after reflection 1 on the slope will impinge onto the slope with an incident horizontal angle $\phi_{i2} = -\phi_{r1}$. The following bottom reflection gives also $\phi_{i3} = -\phi_{r2}$. One thus realizes that, with respect to reflection 3, reflection 2 leads to an increase of the angle ϕ, contributing to untrapping. Consequently, the normalized velocity component v_x does not converge anymore monotonically towards 0, as shown in Fig. 17. As Fig. 16 shows, $\phi_{i,4} = \phi'_{i,3} = \pi + \phi_{r,3} < \phi_{i,1}$ testifying the net focusing after three reflections.

Apart from reflections on vertical or horizontal boundaries, that do not affect v_x, one detects two kinds of reflections. Reflections 1 and 3, that lead to a decrease of v_x in absolute value and reflection 2 that, on the contrary, leads to an increase. Having twice more focusing than defocusing reflections, the angle converges nevertheless towards the fixed point $\phi^\star = 0$.

The combination of reflections 1 and 2 compensate exactly and leave the velocity component v_x unchanged, contrary to reflection 3, the inverse of the convergence time γ_p is given by Eq. (3.5) multiplied by a factor 1/3; only one third of the reflections lead to a decrease of the velocity.

As in the two-dimensional case, attractors exist generically for any parameter values. Although some singular values do not lead

to attractors, one cannot get them experimentally or numerically anyway. As we shall see, one can however not claim that trapping will always occur in 3D since, as already discovered for the (1,3) attractor, trapping and ensuing focusing can be significantly slowed down and even sometimes not occur at all. The example of (2,1) global resonance discussed above is an example of such a case.

3.4. Non trapping cases

3.4.1. $(m, 2)$ attractors

As shown by Fig. 15, a series of reflections 1-2-…-1-2 would give rise to a $(m, 2)$ attractor … that does not exist. Indeed, in two dimensions, two reflections on the sloping bottom, one focusing while the other one is symmetrically defocusing, cannot lead towards a limit cycle. On average, rays do not move away from each other: the Lyapunov exponent is zero. It is known [1,15] that such a case appears only for singular parameter values. One can however choose to be as close as possible to such a singular point.

Fig. 18 shows that one gets a (1,2) attractor-like structure. This is actually not a real attractor: First, trapping does not occur, which means that there is no limit cycle, and therefore no possible convergence towards it. Second, this structure is not a steady state. Indeed, after a sufficiently large number of reflections, the ray converges towards a more complicated true attractor (with more focusing than defocusing reflections). However, for these values, the trapping is very slow since the numbers of focusing and defocusing reflections are approximately identical. The limit cycle corresponds indeed to n focusing reflections and $n-1$ defocusing ones, with n large. This is therefore a situation close to the (1,3) attractor, with a much weaker convergence.
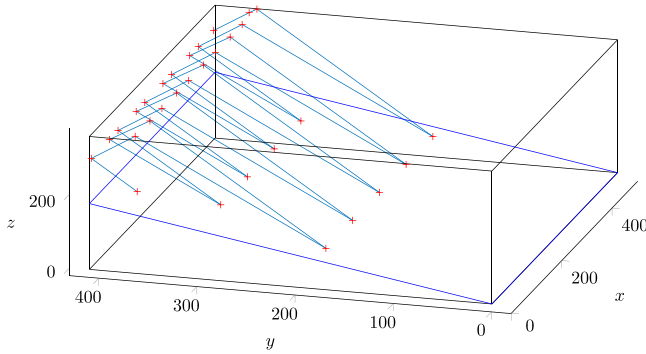
3.4.2. Whispering-gallery modes

Another structure of interest corresponds to geometries for which, for some well chosen initial conditions rays may escape. Similar structures have been identified in a trapezoid, paraboloid, parabolic channel and spherical geometry for internal gravity or inertial wave rays [1,6–8] and are called *whispering gallery modes* in analogy with sound waves. In the system that we study here, such modes exist for very specific parameters and initial conditions: trapping reflections have to be compensated exactly by untrapping ones

Fig. 19 shows the trajectory of one ray in a case that (under normal incidence, $\phi_0 = 0$) should lead to a (1,1) attractor. One can identify a trajectory that is not trapped. It does not visit the full
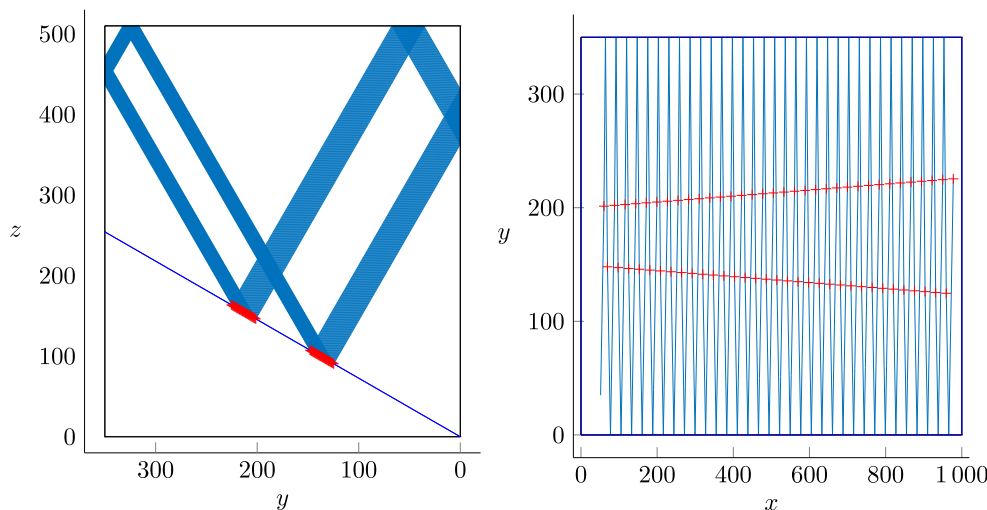
Fig. 18. Side (left panel) and top (right panel) views of a trajectory for a geometry close to a (1,2) attractor that would lead to a vanishing Lyapunov exponent. Reflections on the slope are identified by red crosses.

Fig. 19. Left panel: trajectory of a *whispering-gallery mode* with the initial conditions $\phi_0 = 122.476°$, $x_0 = 0$, $y_0 = 320$, $z_0 = 324$ and the geometrical parameters $H = 360$, $L = 500$, $W = 410$, $\theta = 39°$, $\alpha = 23.52°$. In two-dimensions, this geometry corresponds to the values, $(d = 0.1, \tau = 1.84)$ that leads to a $(1,1)$ attractor. The reflection on the sloping bottom changes ϕ into $-\phi$. After the reflection on the surface and side wall, $y = W$, the successive rays will again impinge onto the slope with $\phi'_i = \phi_i$.

width of the tank, but stays concentrated on one side of the canal. A careful look at the values of ϕ shows that it stays constant, $\phi = \phi_w$ say, if one forgets symmetries with respect to x and y. The value of ϕ_w corresponds to the case for which $\phi_r = -\phi_i$ that leads, as shown in Fig. 19, to $\phi'_i = \pi + \phi_r = \pi - \phi_i$, that explains the stationary state. Using Eq. (2.15), the equality $\phi_r = -\phi_i$ corresponds to

$$\frac{s^2 - 1}{1 + s^2 + 2s \cos \phi_w} = -1, \tag{3.6}$$

that one can simplify in $\phi_w = \pi - \arccos s$ that precisely correspond to the ray tracing value shown in Fig. 19.

Studying the position x_∞ of the trapping plane allows us to identify the existence of whispering-gallery modes that correspond to initial conditions that do not converge. Using the property, shown in Fig. 19, for which the trajectory does not hit the $y = 0$ vertical wall, we are able to make the difference with trajectories that have not converged yet. Fig. 20 presents the result for different initial conditions spanning values of y_0 and ϕ_0 (values of x_0 and z_0 appear to be much less important). The two different panels correspond to x_∞ after two different numbers of reflections. Trajectories that have not converged are identified by the white domains, while colored domains correspond to different positions of the trapping plane.

On the left panel of Fig. 20, one sees that the domain with whispering-gallery modes (white) is very thin: $\phi_0 \in [122.4°, 122.5°]$. The right panel shows that this zone has drastically shrunk even more if one allows 100 times more reflections: most of this domain is therefore not associated with whispering-gallery modes but leads to convergence towards an attractor. It appears finally, that true whispering-gallery modes exist only for singular initial conditions. This is after all, consistent with the theoretical prediction that only one singular value ϕ_w has been found.

The different results presented in this section have emphasized the links between the trapping and the existence of attractors in the two-dimensional transverse geometry. Indeed, as soon as focusing reflections win over defocusing ones in the transverse two-dimensional plane, three-dimensional reflections lead eventually to trapping. As in the geometry under scrutiny, if we omit singular values, attractors exist for any angles (α, θ) and any values H and W: trapping will occur generically. Those singular values are however important. Indeed, as attractors are leading to the focusing of energy, dissipation will significantly reduce their energy. In a given geometrical domain, if the energy is injected in a continuous band of frequencies (i.e. different angles of propagation), the energy will

eventually remain in those that are least dissipated, and therefore in those for which focusing does not occur.

Similarly, although whispering-gallery modes are also the exception rather than the rule, they may be visible in a long enough canal in which the energy in the other frequencies (i.e. for different angles) will be trapped and dissipated in attractors, again because of the focusing mechanism. A far enough measurement in the canal would finally exhibit energy only for frequencies that were not trapped, and therefore not dissipated before. For this reason they have also been termed 'leaky edge waves' [6]: despite their low probability, if they have been excited upstream, whispering-gallery modes will finally show up.

Moreover, experimental measurements will hardly make a difference between a not-yet-converged structure or a whispering-gallery mode: in this sense, Fig. 20(a) is more appropriate than Fig. 20(b). Finally, viscous dissipation was not taken into account in the ray tracing. Although being weak for internal waves that can travel thousands of kilometers [18], the distance that would actually represent the convergence towards the limit cycle of the case discussed in Fig. 18 is far too long to be observed. On the contrary, the transitory quasi-attractor is therefore more likely to be observed (see [19]). In conclusion, from the experimental point of view, only fast trapping cases can be detected.

The key point shown in this section, is that once one knows that there exists an attractor in a two-dimensional geometry, its three-dimensional generalization, obtained by translation of the 2D geometry along an axis orthogonal to z, will inevitably trap rays during their propagation.

In order to consider more realistic bathymetry, we will now study a tridimensional geometry that cannot be obtained by the translation of a 2D geometry.

4. A fully tridimensional geometry with super-attractors

4.1. Choice of the geometry

While all geometries that we studied so far were translationally invariant along the length of the canal (or in other studies rotationally invariant), let us now study a really tridimensional geometry, in which the transverse geometry will vary along the canal. Fig. 21 shows the slope, represented by the blue rectangle, that has been obtained from the one shown in Fig. 8 after an additional rotation with an angle β with respect to the y-axis. In addition to its theoretical interest that we will discuss below, such a study is of course closer to a realistic configuration than previous ones.

Even if one still uses the angle ϕ of a ray with respect to the y-axis, one has to modify the expression of the map linking the reflected angle ϕ_r as a function of the incident one ϕ_i. Indeed, if the trapping effect has the tendency to align the angle of propagation ϕ along the slope of the gradient, the latter is not along the y-direction, but along a direction rotated by an angle ψ with respect to the y-axis, defined as $\tan \psi = -\tan \beta / \tan \alpha$ (see Fig. 21).

With this modification taken into account, formula (2.15) has to be rewritten as

$$\sin(\phi_r - \psi) = \frac{(s^2 - 1) \sin(\phi_i - \psi)}{(1 + s^2) + 2s \cos(\phi_i - \psi)}. \tag{4.1}$$

The associated map, that we will call $\mathcal{R}_\psi$, always has a fixed point corresponding to $\phi^* = \psi$.

4.2. Trapping conditions

Despite the new reflection law (4.1), trapping will still occur. A wave in the transverse yz-plane will have the tendency to align with the upslope-directed gradient. If, in previous geometries,
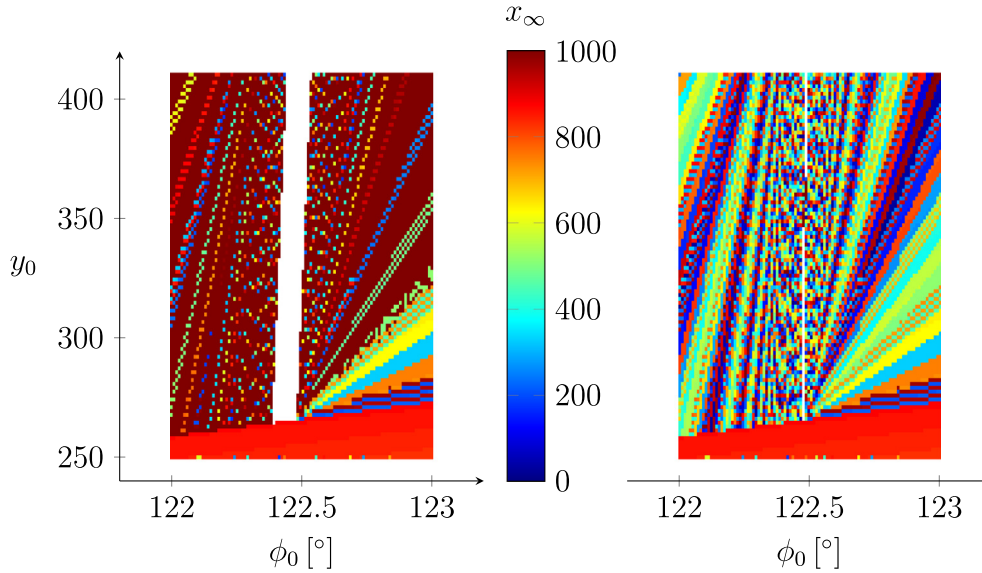
Fig. 20. Position x_∞ of the trapping plane for different initial conditions y_0 and ϕ_0. Left (resp. right) panel presents the value after $N = 10^4$ (resp. $N = 10^6$) reflections. White regions that correspond to domains in which the iteration has not converged correspond to the *whispering-gallery modes*.
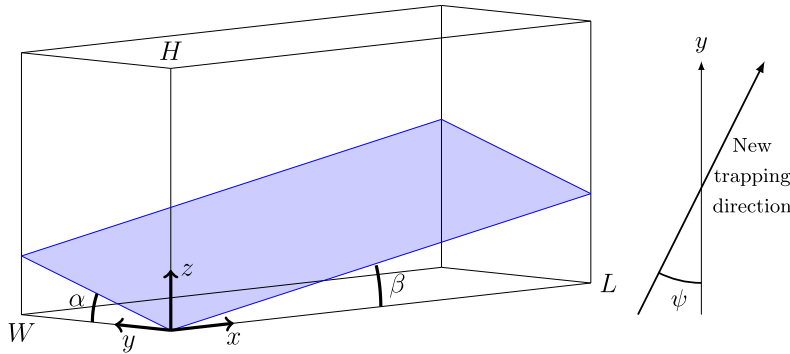
Fig. 21. Geometry under investigation with the definition of the height H, length L and width W of the canal. The slope, represented by the blue rectangle, is now inclined with an angle α with respect to the y-axis and with an angle β with respect to the y-axis. Right panel shows the rotated angle relative to y, which points in true downslope direction.

vertical walls $y = 0$ and $y = L$ were oriented perpendicularly to the trapping direction, this is not the case any more with this geometry. On the contrary, a wave corresponding to $\phi_i = \psi$, will lead (after three successive reflections on a vertical wall, the free surface and a vertical wall like in Fig. 3a) to a bounce on the slope with $\phi'_i = -\psi$, that will untrap the wave.

From this simple remark, one can immediately deduce that two-dimensional attractors are therefore not possible in this geometry. More generally, it is also straightforward to realize that, in three dimensions, an internal wave can converge towards a two-dimensional plane only if the upslope-directed gradient belongs to this plane, while the vertical walls are perpendicular to it. In the geometry under scrutiny, if the walls are perpendicular to the upslope-directed gradient, one recovers the canal geometry studied in the previous section. One thus gets that two-dimensional attractors can be found only when $\psi = 0$, i.e. for $\beta = 0$ as studied in Section 3.

However, the above remark does not prohibit the existence of attractors in domains having tri-dimensional geometries. Such issue is far more complicated and we will now give some new insight along this line.

4.3. Tri-dimensional super-attractors

Despite the impossibility to get two-dimensional attractors, one can consider cases for which the transverse geometry is close to the one with a (1,1) attractor in 2D. Intuitively, if three dimensional structures do exist, they should have a few rebounds and be therefore easier to handle. Let us exhibit such a tridimensional structure for a given set of parameters.
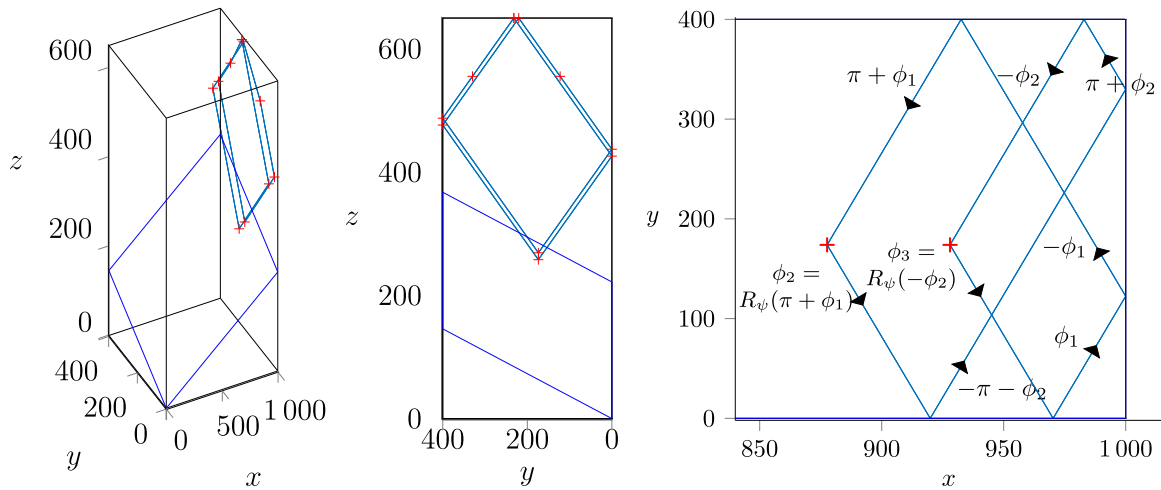
Fig. 22 presents the stationary structure that one gets with different views. As shown by the left panel, the structure is confined close to the end of the canal $x = L$, while the side view is strongly reminiscent of a (1,1) attractor. On the contrary, the top view emphasizes its three-dimensional nature, with two different reflections on the inclined slope.

The successive reflections and the different angles of propagation have been plotted on the right panel of Fig. 22. Calling ϕ_1 the initial angle, the incident beam hits the walls $x = L$ and $y = W$, before impinging onto the inclined slope. The reflected angle is therefore $\phi_2 = \mathcal{R}_\psi(\pi + \phi_1)$. After three reflections on the vertical walls the second reflection on the slope occurs, leading to an angle of propagation $\phi_3 = \mathcal{R}_\psi(-\phi_2)$ that has to be equal to $-\pi - \phi_1$ so that the cycle will start again. One thus ends with an angle ϕ_1 that fulfills the following equation

$$\phi_1 = -\pi - \mathcal{R}_\psi(-\phi_2) \tag{4.2}$$

$$= -\pi - \mathcal{R}_\psi(-\mathcal{R}_\psi(\pi + \phi_1)). \tag{4.3}$$

Finding a fixed point of this equation is not easy to exhibit analytically since $\mathcal{R}_\psi(-\phi)$ cannot be simplified since ψ breaks the symmetry with respect to the y-axis. Using the ray tracing approach,

Fig. 22. Stationary structure in the tri-dimensional case with $H = 650$, $L = 1000$, $W = 400$, $\theta = 43.2°$, $\alpha = 20°$ and $\beta = 12.5°$. The left (resp. centered, right) panel presents a perspective (resp. side, top) view. Red crosses refer to reflections from boundaries (left and middle panels), or sloping bottom (right panel).

one can find the fixed point $\phi^* \simeq -14°$. The next reflection on the vertical wall leads to an untrapping that is exactly compensated by the following reflection on the slope. These steps are detailed in Fig. 22c.

Fig. 23 presents the different stationary structures that one obtains by varying either ϕ_0 (left panel) or y_0 and z_0 (right panel). Although leading to different stationary structures, one always gets a limit cycle with two reflections off the wall at $x = L$, similar to the structure shown in Fig. 22. Such a behavior is different from the attractors obtained in the simpler canal geometry discussed in previous section.

Despite the small variations in the bouncing coordinates, the limit cycle is almost unchanged for all initial conditions. One thus gets a situation close to the two-dimensional one, with the difference that they occur only close to the end wall $x = L$. The change of the geometry in the longitudinal direction of the canal has important consequences: trapping regions that were possible all along the translationally invariant canal, are now confined to the region close to the end of a canal that is not translationally invariant. This is therefore a "super-attractor" since the energy is trapped in a significantly more restricted region.

In the example discussed above, only one reflection is sufficient to make a significant change in the angle of propagation. However, for lower values of s and larger values of ψ, the wave can be trapped after several reflections. Using similar ideas, it is therefore possible to exhibit even more complicated structures, with progressive trapping with reflections on the slope and untrapping on the wall $x = L$ [15].

5. Conclusion

In this paper, we have shown that although the dispersion relation is unchanged, the propagation in three dimensions is significantly more complicated than its two-dimensional version. The wave propagation on a cone that generalizes the Saint Andrew's cross justifies the introduction of an additional angle of propagation ϕ that allows to describe the position of a wave ray in the horizontal plane.

We have studied the evolution of this reflection angle over inclined slopes and shown the emergence of a new mechanism that has the tendency to align this angle ϕ with the upslope gradient. We have also carefully studied this trapping in the rather simple geometry of a translationally invariant canal. This configuration leads to a trapezium very similar to what has been extensively studied in two-dimensions. It is however important to emphasize

that we also established a direct link between the trapping and the existence of two-dimensional attractors. The important feature is that, in such a case, there is not only one attractor that would attract all rays, but an infinity of two-dimensional attractors distributed along the canal, that we refer to as a two-dimensional attracting manifold.

We have also considered a geometry that is not translationally invariant which is closer to realistic configurations. In this new geometry, we were able to prove that there are no two-dimensional attractors. However, we have exhibited a three-dimensional structure with properties similar to internal wave attractors. Moreover, as it is unique, it is likely that it should be easy to visualize it in laboratory experiments since the energy injected in the domain would be eventually confined to a very thin region in three-dimensional space: a *one*-dimensional manifold, which is the reason for calling it a super-attractor. The experimental verification of this prediction is one of our priorities.

As a side remark, we note that translational invariance is of course broken at the front and end walls of the canal where frictional effects might modify the attracting structures [20]. For internal gravity waves, having rectilinear particle motions, this is not seen as leading to major changes. But for the analogous case of inertial waves, that possess (inclined) *circular* particle motions this is an issue, and adjustment at an inviscid level is to be expected. A preliminary experimental study of the attracting two-dimensional manifold of inertial waves does indeed show adjustment of the cross-sectional attractor shape on approach of the side walls [8].

The study of attractors in three dimensions is however still in its infancy and we expect other very interesting features to discover. Considering more complicated attractors in even more realistic configurations is important. Moreover, the existence and the likelihood of super-attractors in generic three dimensional geometry is fully open and could lead to interesting predictions when considering the real bathymetry of oceans: that should lead the way for observations in the oceans.
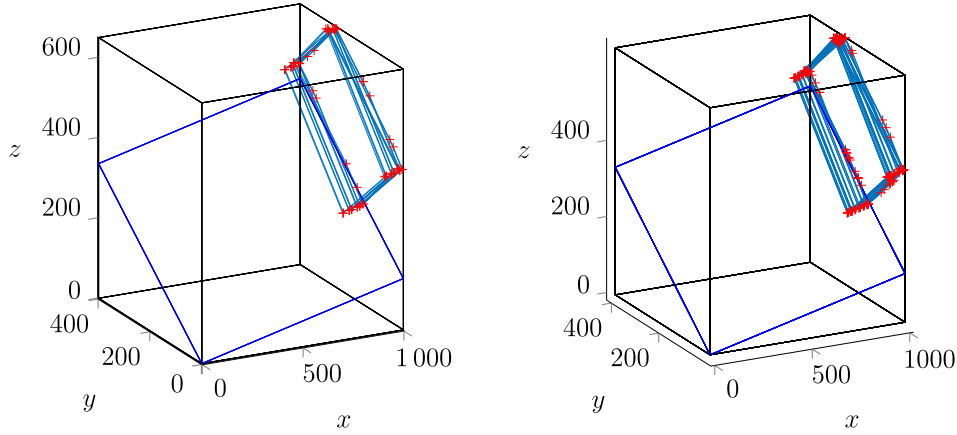
Fig. 23. Three-dimensional attractors obtained for different initial conditions, varying $\phi_0 \in [-80°, 80°]$ (left panel) or varying $y_0 \in [0, W]$ and $z_0 \in [0, H]$ (right panel). All other parameters are those given in the caption of Fig. 22.

Appendix

The incident and reflected velocity fields share a reciprocal relationship as they should switch role upon time-reversal. This is borne out when rewriting Eqs. (2.10) and (2.11) as

$$\begin{pmatrix} -s & 1 \\ 1 & -s \end{pmatrix} \begin{pmatrix} v_y \\ v_z \end{pmatrix}_r = \begin{pmatrix} s & -1 \\ 1 & -s \end{pmatrix} \begin{pmatrix} v_y \\ v_z \end{pmatrix}_i \qquad (A.1)$$

or, employing the projection of the velocity vector onto the plane perpendicular to the sloping topography, $\vec{v}_\perp = (v_y, v_z)$,

$$P\vec{v}_{\perp,r} = Q\vec{v}_{\perp,i},$$

where we use unimodular matrices that have determinant ± 1:

$$P \equiv \frac{1}{\sqrt{1-s^2}} \begin{pmatrix} -s & 1 \\ 1 & -s \end{pmatrix}, \qquad Q \equiv \frac{1}{\sqrt{1-s^2}} \begin{pmatrix} s & -1 \\ 1 & -s \end{pmatrix}.$$

Interestingly, these hyperbolic matrices reflect their reciprocal nature by obeying the identity

$$P^{-1}Q = Q^{-1}P \equiv R,$$

which implies

$$\vec{v}_{\perp,r} = R\vec{v}_{\perp,i}, \quad \text{and} \quad \vec{v}_{\perp,i} = R\vec{v}_{\perp,r}.$$

The matrices acquire standard form when, for subcritical slope, $s < 1$, we write $s = \tanh \nu$, so that

$$P \equiv \begin{pmatrix} -\sinh \nu & \cosh \nu \\ \cosh \nu & -\sinh \nu \end{pmatrix} \quad \text{and} \quad Q \equiv \begin{pmatrix} \sinh \nu & -\cosh \nu \\ \cosh \nu & -\sinh \nu \end{pmatrix}. \tag{A.2}$$

Notice that $\det(P) = -1$ and $\det(Q) = 1$.

For supercritical topography, $s > 1$, we premultiply left and right hand sides of (A.1) by $-1/\sqrt{s^2 - 1}$, and, writing $s = \coth \mu$, we find

$$P \equiv \begin{pmatrix} \cosh \mu & -\sinh \mu \\ -\sinh \mu & \cosh \mu \end{pmatrix} \quad \text{and} \quad Q \equiv \begin{pmatrix} -\cosh \mu & \sinh \mu \\ -\sinh \mu & \cosh \mu \end{pmatrix}.$$

Defining $Q_n = Q(n\mu)$, such that the previously defined $Q \equiv Q_1$, it appears that

$$P^{-1}Q = Q^{-1}P = Q_2.$$

These reciprocal relations are useful when computing the velocity vector upon a ray's reflection from a boundary, given the incident velocity vector. It also helps determining the proper root when solving the multivalued (2.15) for horizontal direction ϕ_r, and subsequent angle of incidence $\phi'_i = \pi + \phi_r$, given the incident angle of incidence ϕ_i and slope s.

For subcritically sloping topography, $s < 1$, with

$$\Phi(\phi, s) \equiv \sin^{-1} \left(\frac{(1-s^2)\sin \phi}{1 + s^2 + 2s\cos \phi} \right),$$

and

$$\varphi(s) \equiv \pi - \sin^{-1} \left(\frac{1-s^2}{1+s^2} \right) = \pi - \Phi\left(\frac{\pi}{2}, s \right),$$

we obtain as subsequent angle of incidence

$$\phi' = \mathcal{R}(\phi, s) \equiv \begin{cases} \pi - \Phi(\phi, s), & \text{if } \phi < -\varphi(s) \\ \Phi(\phi, s), & \text{if } |\phi| < \varphi(s) \\ \pi + \Phi(\phi, s), & \text{if } \phi > \varphi(s), \end{cases}$$

displayed in Fig. 4. The conditions apply to secure continuity when ϕ' passes $\pm \pi/2$.

For supercritical topography, $s > 1$, we need to distinguish between rays incident from above and below. Recalling from Section 2.3.3 that $\phi_\ell(s) = \tan^{-1}\sqrt{s^2 - 1}$, for rays incident from above ($v_{z,i} < 0$), we find

$$\phi' = \mathcal{R}(\phi, s) \equiv -\Phi(\phi, s) \text{ if } -\pi + \phi_\ell(s) \leq \phi \leq \pi - \phi_\ell(s),$$

displayed in Fig. 6a, while for rays incident from below ($v_{z,i} > 0$), i.e. for $-\phi_\ell(s) \leq \phi \leq \phi_\ell(s)$, we have the reciprocal relation

$$\phi' = \mathcal{R}(\phi, s) \equiv \begin{cases} -\pi + \Phi(\phi, -s), & \text{if } \phi < \pi - \varphi(s) \\ -\Phi(\phi, -s), & \text{if } |\phi| < \varphi(s) - \pi \\ \pi + \Phi(\phi, -s), & \text{if } \phi > \varphi(s) - \pi, \end{cases}$$

displayed in Fig. 6b.

References

[1] L.R.M. Maas, Wave attractors: linear yet nonlinear Int, J. Bifurcat. Chaos 15 (9) (2005) 2757–2782.

[2] A. Rabitti, L.R.M. Maas, Meridional trapping and zonal propagation of inertial waves in a rotating fluid shell, J. Fluid Mech. 729 (2013) 445–470.

[3] M. Rieutord, B. Georgeot, Valdettaro, Inertial waves in a rotating spherical shell: attractors and asymptotic spectrum, J. Fluid Mech. 435 (2001) 103–144.

[4] B. Dintrans, M. Rieutord, L. Valdettaro, Gravito-inertial waves in a rotating stratified sphere or spherical shell, J. Fluid Mech. 398 (1999) 271–297.

[5] Q. André, A.J. Barker, S. Mathis, Layered semi-convection and tides in giant planet interior. arXiv:1710.10058, 2017.

[6] S. Drijfhout, L.R.M. Maas, Impact of channel geometry and rotation on the trapping of internal tides, J. Phys. Oc. 37 (2007) 2740–2763.

[7] A. Rabitti, L.R.M. Maas, Inertial wave rays in rotating spherical fluid domains, J. Fluid Mech. 758 (2014) 621–654.

[8] A.M.M. Manders, L.R.M. Maas, On the three-dimensional structure of the inertial wave field in a rectangular basin with one sloping boundary, Fluid Dyn. Res. 35 (2004) 1–21.

[9] M.I. El-Sabh, N. Silverberg, Coastal and Estuarine Studies. Oceanography of a Large-Scale Estuarine System: The St. Lawrence, Springer-Verlag, 1990.

[10] F. Cyr, D. Bourgault, P.S. Galbraith, Behavior and mixing of a cold intermediate layer near a sloping boundary, Ocean Dyn. 65 (2015) 357–374.

[11] J. Wang, R.G. Ingram, L.A. Mysak, Variability of internal tides in the laurentian channel, J. Geophys. Res. 96 (16) (1991) 859–16875.

[12] L.R.M. Maas, F.P.A. Lam, Geometric focusing of internal waves, J. Fluid Mech. 300 (1995) 1–41.

[13] C. Brouzet, I.N. Sibgatullin, H. Scolan, E.V. Ermanyuk, T. Dauxois, Internal wave attractors examined using laboratory experiments and 3D numerical simulations, J. Fluid Mech. 793 (2016) 109–131.

[14] C. Brouzet, Internal Wave Attractors: from Geometrical Focusing to Nonlinear Energy Cascade and Mixing (Ph.D. thesis), ENS de Lyon, 2016.

[15] G. Pillet, Attracteurs D'Ondes Internes à Trois Dimensions : Analyse Par Tracés de Rayons Et étude Expérimentale (Ph.D. thesis), ENS de Lyon, 2018.

[16] L.R.M. Maas, Exact analytic self-similar solution of a wave attractor field, Physica D 238 (5) (2009) 502–505.

[17] C. Brouzet, E. Ermanyuk, S. Joubaud, G. Pillet, T. Dauxois, Internal wave attractors: different scenarios of instability, J. Fluid Mech. 811 (2017) 544–568.

[18] R.D. Ray, G.T. Mitchum, Surface manifestation of internal tides in the deep ocean: observations from altimetry and island gauges, Prog. Oceanogr. 40 (1997) 135–162.

[19] G. Pillet, E. Ermanyuk, L. Maas, I. Sibgatullin, T. Dauxois, Internal wave attractors in three-dimensional geometries: trapping by oblique reflection, J. Fluid Mech. 845 (2018) 203–225.

[20] F. Beckebanze, C. Brouzet, I.N. Sibgatullin, L.R.M. Maas, Damping of quasi-two-dimensional internal wave attractors by rigid-wall friction, J. Fluid Mech. 841 (2018) 614–635.